

Annealing Effect on the Shape Memory Properties of Amorphous NiTi Thin Films

Gen Satoh

e-mail: gs2358@columbia.edu

Andrew Birnbaum

e-mail: ajb2118@columbia.edu

Y. Lawrence Yao

e-mail: yly1@columbia.edu

Department of Mechanical Engineering,
Columbia University,
New York, NY 10025

Thin film shape memory alloys have recently become a promising material for the actuation of devices on the microscale such as micropumps and microvalves. Their utilization, however, has been limited due to the difficulty in tailoring their properties for different applications. Control over the transformation temperatures as well as mechanical and shape memory properties is required to enable their widespread use. This study examines the effects of heat treatment time and temperature on the properties of amorphous, Ti-rich NiTi thin films on silicon substrates. The effects on the transformation temperatures are investigated through the use of temperature dependent optical microscopy and temperature dependent X-ray diffraction. The indentation modulus and hardness, as well as dissipated energy and depth recovery, are obtained through nanoindentation and atomic force microscopy. The role of microstructure and composition in altering both the mechanical and shape memory properties of the films is discussed.

[DOI: 10.1115/1.4002189]

1 Introduction

Originally observed in bulk specimens, the shape memory effect (SME) and superelasticity (SE) are characteristics shared by the class of materials called shape memory alloys (SMAs). These materials generated a great deal of interest in their infancy due to their ability to recover large deformations upon heating and to endure significant, seemingly elastic strains. Recently, thin film shape memory alloys have gained popularity due to their small thermal mass and thus fast response time and are of particular interest for use in microelectromechanical devices (MEMS) as actuators due to their ability to produce large forces and displacements. One particular SMA, NiTi, has been the focus of extensive research for biomedical applications due to its excellent biocompatibility and good shape memory characteristics. NiTi thin films have been applied to various MEMS applications such as microgrippers and microvalves [1].

Crystallization of the amorphous thin films produced through sputtering is typically performed by furnace annealing. Furnace annealing of thin film specimens has been shown to produce specimens that exhibit shape memory properties comparable to those of bulk materials [2]. Lee et al. [3] characterized the nucleation and growth of NiTi crystals in amorphous sputtered films through in situ transmission electron microscopy (TEM) observation. Furthermore, control over transformation temperature, recoverable strain, and even biocompatibility has been demonstrated by varying annealing parameters and deposition conditions [4–6]. These works, however, are limited to a small set of annealing temperatures and times and are unable to observe the transition between superelastic and shape memory material responses for different heat treatments.

X-ray diffraction (XRD) and TEM, among others, have been the primary methods by which both bulk and thin film SMAs have been characterized. These methods have been used to determine the crystal structure, phase transformation temperatures, and precipitation behavior of annealed specimens. The increased interest in thin film SMA also requires the use of different characterization methods that can accurately test materials in this form. Recent

studies of the micro- and nanoscale properties of SMA such as NiTi have made use of nanoindentation for this purpose. Gall et al. [7] studied the nanoindentation response of bulk, Ni-rich, superelastic, single crystal NiTi in different orientations. Nanoindentation of thin films has also been used to determine the mechanical properties of sputtered and annealed films as a function of composition and film thickness [8,9]. Nanoindentation is particularly appealing for thin film specimens since they are not easily characterized by conventional means. Amorphous, Ti-rich materials are of particular interest when considering thin films since they form microstructures unattainable in bulk materials [10]. There remains to be, however, a systematic study on the effects of heat treatment, specifically temperature and dwell time, on the nanoindentation response of thin film Ti-rich NiTi.

In this study, the effects of aging heat treatments on amorphous, sputtered, Ti-rich NiTi films are examined to provide insight into the evolution of their microstructures and shape memory properties. Specifically, the effects of annealing temperature and dwell time on the transformation temperatures and mechanical and shape memory properties are characterized through the use of optical microscopy, X-ray diffraction, nanoindentation, and atomic force microscopy (AFM) measurements.

2 Background

2.1 Shape Memory and Superelasticity. The SME and SE exhibited by shape memory alloys are both manifestations of a reversible crystallographic shift known as the martensitic transformation. A brief description of shape memory phase transformations and some key relations is included in this section to support a discussion of the experimental results.

Thermodynamically, the driving force for the transformation is the change in free energy between the austenite and martensite structures where the free energy for each phase can be written as [11]

$$G^* = U + PV - TS - Fl = H^* - TS \quad (1)$$

where U , P , V , T , S , F , and l are the internal energy, pressure, volume, temperature, entropy, force applied to the specimen, and change in length of the specimen, respectively. The enthalpy component of the free energy is denoted as H^* . At the equilibrium temperature, the free energy of martensite is equal to that of the austenite, which gives the following relation at constant pressure:

Contributed by the Manufacturing Engineering Division of ASME for publication in the JOURNAL OF MANUFACTURING SCIENCE AND ENGINEERING. Manuscript received June 22, 2009; final manuscript received July 1, 2010; published online September 20, 2010. Assoc. Editor: Bin Wei.

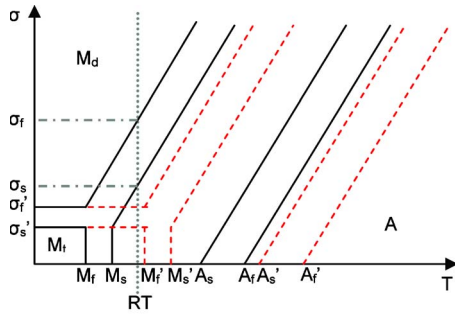


Fig. 1 Schematic diagram of the stress-temperature phase diagram for NiTi

$$dG^{*A} = dG^{*M} = -S^A dT - l^A dF = -S^M dT - l^M dF \quad (2)$$

where the superscripts *A* and *M* indicate the values for austenite and martensite, respectively. Therefore, at the equilibrium temperature and constant pressure,

$$\frac{d\sigma}{dT} = -\frac{\Delta S^{A \rightarrow M}}{\varepsilon^{A \rightarrow M}} = -\frac{\Delta H^{*A \rightarrow M}}{T_o(\sigma)\varepsilon^{A \rightarrow M}} \quad (3)$$

Equation (3) is the Clausius–Clapeyron relationship for stress and temperature for the phase transition between austenite and martensite and quantifies the change in the equilibrium temperature, T_o , with applied stress and conversely changes in the stress required to induce the phase transformation with changes in the equilibrium temperature. Equation (3) is used to define the slope of the lines delineating the phase regions in the schematic phase diagram of NiTi in the stress-temperature domain (Fig. 1).

Figure 1 shows the effects of changes in transformation temperature on the stresses required to initiate and complete the phase transformations, denoted as σ_s and σ_f . The material depicted by the dashed lines is composed of twinned martensite at room temperature and is fully transformed to detwinned martensite at a stress of σ_f' . The material depicted by the solid lines, however, could be martensitic or austenitic at room temperature and will not complete its transformation to detwinned martensite until a larger stress, σ_f , is reached. All else being constant, these changes in the phase transformation temperatures of the materials can significantly affect their responses to mechanical loading by causing either the shape memory or the superelastic response to be active.

In addition to changes between the shape memory and superelastic responses, adjustment of phase transformation temperatures can cause complete loss of shape memory properties if the stress required to initiate the phase transformation becomes too large. For simplicity, we define the critical stress to induce the phase transformation as a single value, σ_{mr} , and σ_Y as the yield stress. Materials with $\sigma_{mr} > \sigma_Y$ will exhibit a conventional elastic-plastic response with no shape memory or superelastic properties. Since the yield stress is below the critical stress, deformation will be accommodated by plasticity before any phase transformation takes place. Materials with $\sigma_{mr} < \sigma_Y$ will undergo a phase transformation upon loading before reaching plasticity and, depending on the transformation temperatures at zero stress, will exhibit shape memory or superelastic properties.

2.2 Indentation and Depth Recovery. Under complex loading conditions such as those caused by indentation, a mixture of deformation accommodated by phase transformation and deformation accommodated by plasticity is typically seen due to non-uniform stress distributions in the material. Modeling of this process begins with Hill [12], who used an expanding cavity model to determine the radial displacement, $u(r)$, of material surrounding an expanding hemispherical cavity

$$u(r) = \frac{Y_{pl} r}{E} \left[(1 - \nu) \frac{c_{pl}^3}{r^3} - \frac{2}{3} (1 - 2\nu) - 2(1 - 2\nu) \ln \left(\frac{c_{pl}}{r} \right) \right] \quad (4)$$

where Y_{pl} is the yield stress, E is Young's modulus, c_{pl} is the radius of the elastic-plastic interface, and ν is Poisson's ratio. Johnson [13] applied this model to the displacements produced by a conical indenter, which have been shown to be radial with contours being roughly hemispherical in shape. Taking the derivative of Eq. (4) with respect to c and conserving volume as the indenter tip is pushed into the material, the radius of the plastically deformed region can be defined as

$$c_{pl} = \frac{d}{\tan \beta} \left[\frac{E \tan \beta}{6Y_{pl}(1 - \nu)} + \frac{2 - 4\nu}{3 - 3\nu} \right]^{1/3} \quad (5)$$

where d is the indentation depth and β is the angle between the indenter face and the film surface (19.7 deg for the equivalent cone for a Berkovich indenter). Similarly, by replacing Y_{pl} with Y_{mr} , the critical stress to induce detwinning of martensite, the radius of the shape memory region, c_{mr} , can be determined. Following Shaw et al. [14], since only the material within the shape memory region and outside the plastic region recovers when heated and assuming constant modulus and Poisson's ratio, the theoretical depth recovery ratio, R_{th} , of a martensitic film under indentation by a conical indenter tip can be determined,

$$R_{th} = \frac{c_{mr} - c_{pl}}{c_{mr}} \approx 1 - \left(\frac{Y_{mr}}{Y_{pl}} \right)^{1/3} \quad (6)$$

This relationship illustrates the importance of these critical stresses on the material response of the films.

3 Experimental Procedure

Ti-rich Ti–Ni thin films were deposited on silicon substrates with a 1 μm ultralow residual stress Si_3N_4 plasma enhanced chemical vapor deposition (PECVD) barrier layer to prevent any interaction between the film and substrate. The films were deposited at room temperature in a magnetron sputtering system from an equiatomic NiTi target and a pure Ti target to achieve an amorphous structure. The composition of the film was determined by energy-dispersive X-ray spectroscopy (EDX) to be 51.8 at. % Ti–Ni, and the film thickness was 1 μm . Annealing of the films was performed in a vacuum tube furnace with proportional-integral-derivative (PID) control. The specimens were placed in the furnace at the annealing temperature, and a slight flow of ultrahigh purity argon was maintained throughout the annealing time. The system was also evacuated using a vacuum pump after insertion of the sample to reduce the oxygen levels in the tube. To further reduce oxidation during annealing, the NiTi film was placed against a small quartz plate, and both pieces were enclosed in a stainless steel foil pouch.

Classical heat treatments of alloys consist of a solution treatment followed by an aging step. As shown in Fig. 2, the maximum solubility limit for Ti in NiTi is 50.5 at. %, and thus the film used for these experiments (51.8 at. % Ti–Ni) will not form a stable solid solution at any temperature [14]. Since the sputter deposited Ti-rich film has an unstable, homogeneous composition similar to a quenched solid solution, no solution treatment step was performed prior to aging. Aging treatments were performed at four different temperatures: 460°C, 560°C, 660°C, and 760°C with durations of 5 min, 30 min, and 60 min. After aging, the samples were quenched in water to stop the precipitation process.

Following the aging treatment, the films were characterized using optical microscopy with a differential interference contrast (DIC) apparatus and a heating/cooling stage. The DIC system enhances the contrast in the image through optical interference and allows for much clearer imaging of the surface of the NiTi films. Using this system, along with the heating and cooling capabilities, allows optical measurements of the phase transformation tempera-

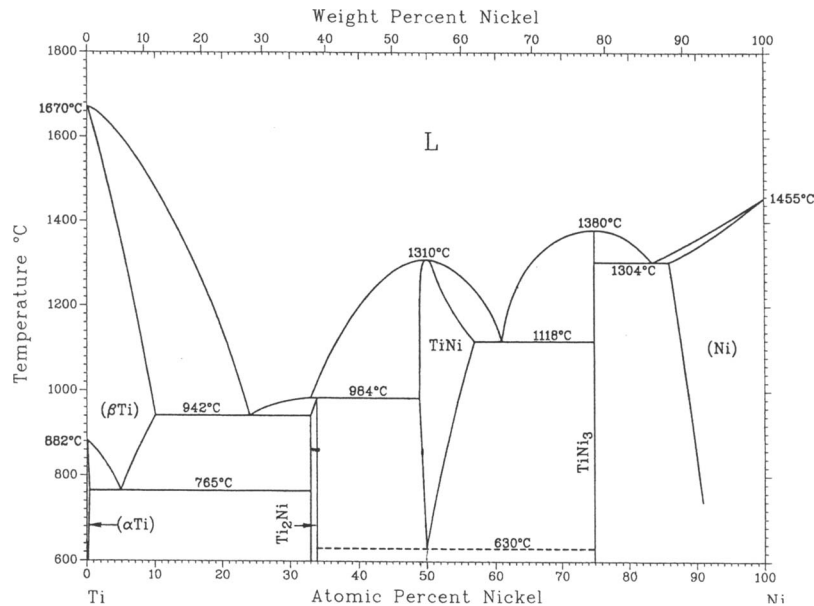


Fig. 2 NiTi phase diagram. Note near-constant solubility limit of Ti on Ti-rich side of NiTi [20].

tures by observing the disappearance and reappearance of the martensitic surface relief upon changes in temperature.

In situ temperature dependent X-ray diffraction measurements were also performed on the annealed specimens to determine the room temperature phase and transformation temperatures of the film. By observing the growth and decay of the austenitic peaks in the XRD spectrum with changes in temperature, the phase transformation temperatures can be identified. The growth of the peaks begins at the austenitic start temperature and ends at the austenitic finish temperature, while decay of the peaks begins at the martensitic start temperature and ends at the martensitic finish temperature.

The heating and cooling stage for both the in situ temperature dependent optical microscopy and X-ray diffraction measurements consisted of a water-cooled Peltier module. Heating and cooling were achieved using the same device by switching the polarity of the supply voltage. Temperatures were measured using a thermocouple that was placed on the surface of a second, identical sample situated nearby on the thermoelectric device to minimize interference with imaging and diffraction measurements.

Nanoindentation was used as a means to determine the shape memory and mechanical properties of the annealed thin films. A diamond Berkovich tip was used. Two types of indentation tests were performed on the annealed specimens. For the first type, the basic indentation test, the indentation modulus, and the hardness of the films are calculated at a specified displacement into the film. The second type is the continuous stiffness measurement (CSM). By applying a small oscillating load over the basic load curve, local unloading can be achieved at each increment in indentation depth, and material properties can be measured as a function of depth into the surface. CSM measurements were performed to a depth of 1 μm to characterize the full thickness of the film. Basic tests were performed to a depth of 100 nm to minimize substrate effects on the material response. The basic indentations were subsequently imaged using an atomic force microscope to determine their initial depth, D_{max} , and measured again after being heated above their austenitic finish temperatures to determine the recovered depth, D_r . The recovery ratio, defined as $\Phi = (D_{\text{max}} - D_r) / D_{\text{max}}$, represents the level of deformation accommodated by detwinning and phase transformations and is analogous to Eq. (6).

4 Results and Discussion

Among the many factors that influence the mechanical and shape memory properties of NiTi films is the microstructure of the material, more specifically, the size and types of precipitates. Ti-rich NiTi has been shown to develop NiTi₂ precipitates; however, due to the maximum solubility of Ti in NiTi being only 50.5 at. %, in bulk materials NiTi₂ precipitates only form at grain boundaries, which limits their effectiveness in changing the properties of the material. Sputter deposition of Ti-rich NiTi thin films, however, is able to create an unstable structure with a homogeneous distribution of Ti no matter what the composition is. The subsequent aging of these films causes precipitates to form within the NiTi grains, which initially form as thin plates or Guinier-Preston (GP) zones at low annealing temperatures and times [10]. These plate precipitates are coherent with the austenite matrix, and their coherency strains strengthen the austenite phase. Increases in the annealing temperature or time have been shown to cause the precipitates to become spherical in shape and lose their coherency with the austenite matrix resulting in a decreased critical stress for slip.

4.1 Surface Relief Length. The surface relief caused by martensitic variant formation is seen clearly with the use of DIC optical microscopy, as shown in Figs. 3(b) and 3(c). The length of these plates has been reported to be affected by a number of variables such as grain size and precipitation. More specifically, Zhang et al. [15] showed that martensitic plates growing in an austenitic matrix are unable to pass through the larger, spherical precipitates that form at higher temperatures and longer annealing times but are undeterred by the smaller, coherent GP zones that form at lower temperatures and shorter annealing times. Additionally, the high concentration of dislocations surrounding the incoherent precipitates is thought to encourage the nucleation of martensites. Thus, the films that contain only GP zones should have the longest plates, which would decrease in length as the GP zones grew into spherical precipitates.

The measured martensite lengths for films annealed at 460°C and 560°C are shown in Fig. 3(a) as a function of time. There is little change in the lengths between the samples annealed for 5 min and 30 min at 460°C; however, the lengths begin to decrease

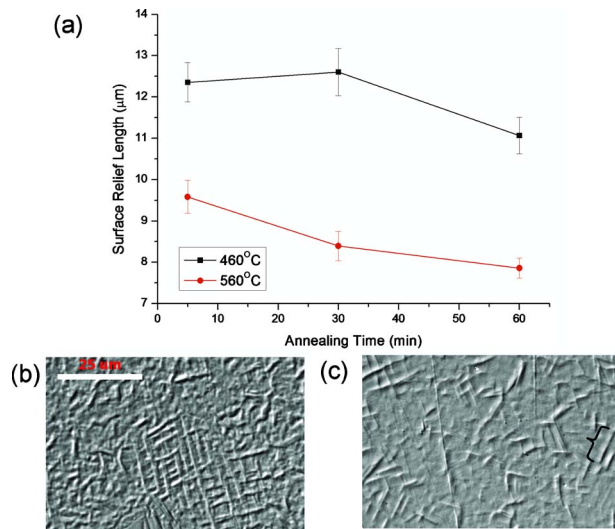


Fig. 3 (a) Length of martensitic surface relief as a function of annealing parameters. Error bars denote standard error. Optical micrographs of samples annealed at (b) 460°C for 5 min and (c) 560°C for 60 min (surface relief length denoted by bracket).

for the 60 min annealing time. The surface relief lengths for the samples annealed at 560°C are still shorter and show a similar trend of decreasing length with annealing time. This behavior is expected due to the increase in diffusion rate at higher temperatures and greater time for diffusion to occur for longer anneals. Both of these relationships have the effect of allowing for greater growth of the precipitates from the initial GP zones to larger spherical precipitates. As the spherical precipitates begin to form, the maximum plate length is reduced due to their inability to grow through those regions. Ishida et al. [16] also showed that there is a transition region between materials containing GP zones and those with spherical precipitates where a mixture of the two types of precipitates is observed. This observation qualitatively agrees with our experimental data, which show a gradual decrease in plate length with increasing annealing temperature and time.

While precipitate formation is one factor in determining the plate size, grain size also has an effect on the maximum size due to the fact that the plates generally do not grow through grain boundaries. This suggests that a decreasing grain size could also be the reason for the observed decrease in plate length with time and temperature. However, it was observed that the maximum plate lengths for the films annealed at 460°C and 560°C were nearly identical, suggesting that the grain size of the films is not changing significantly and is thus not responsible for the observed change in plate length. The films annealed at higher temperatures were austenitic even upon cooling to 5°C, and surface relief length could not be measured.

4.2 Transformation Temperature—Optical. The changes in surface relief of a typical martensitic specimen upon heating and cooling as observed through optical microscopy are shown in Fig. 4. This surface relief is due to the existence of various martensitic variants within the film. As the temperature is increased past the austenitic start temperature, the variants begin to disappear. Upon reaching the austenitic finish temperature, the surface exhibits a smooth surface indicative of austenite. Upon cooling from the elevated temperature, the variants begin to reappear at the martensitic start temperature and have fully developed upon reaching the martensitic finish temperature. By tracking the temperature of the sample and observing the appearance and disappearance of the martensitic variants, a measure of the transformation temperatures of the film can be obtained. Transformation temperatures of films obtained using this method are shown in Table 1. Not all samples

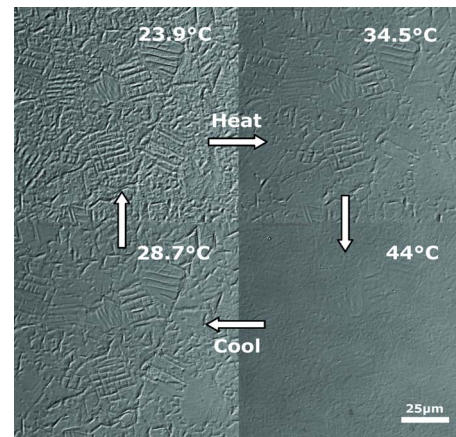


Fig. 4 Representative DIC optical micrographs of a martensitic sample upon heating and cooling

are included in Table 1 since some samples did not undergo any visible transformation even when cooled to 5°C, the limit of the cooling stage used in this experiment. All samples where this was the case were annealed at temperatures above 660°C. This suggests that the transformation temperatures of the surface of the films annealed at elevated temperatures may be below room temperature. It has been reported [17] that the transformation temperatures of NiTi are a strong function of composition, with Ti-rich samples having higher transformation temperatures and decreasing with decreasing Ti content. The effect of annealing temperature on the transformation temperatures for samples annealed for 5 min is shown in Fig. 5. This trend of decreasing transformation temperatures with increasing annealing temperature is attributed to the change in matrix composition and was observed for longer annealing times as well (not shown). The effect of annealing time on the transformation temperatures of samples annealed at 560°C is depicted in Fig. 6 and also shows a decreasing trend.

Since the solubility limit of Ti in NiTi is nearly constant with temperature, the driving force for diffusion for all annealing parameters is similar. Increased annealing time and temperature would allow for greater diffusion within the Ti-rich samples, which could lead to greater precipitation and thus a decrease in the Ti content of the matrix accompanied by the observed decrease in transformation temperatures. The transformation temperatures of samples annealed at 460°C, however, were nearly constant with annealing time, suggesting that the diffusion rate at this temperature is too low to have a significant effect on the matrix composition.

It should also be noted that for the annealing parameters considered in this study, the precipitate shape and size do not seem to have a significant effect on the transformation temperatures of the samples. Ishida et al. [18] reported significant increases in the transformation temperatures of Ti-rich NiTi thin films with annealing time. However, their experiments were performed for much longer times, from 1 h to 100 h, and only spherical NiTi₂ precipitates were observed. Initial diffusion and precipitation rates are high due to the Ti content being greater than the solubility limit in NiTi and are expected to decrease with time and cause the matrix Ti composition to decrease quickly at first. Thus, as observed, the effect of matrix composition should be stronger for shorter annealing times and have less of an effect for extended heat treatments.

4.3 Transformation Temperature—XRD. In situ temperature dependent X-ray diffraction was also used to determine the transformation temperatures of the annealed films. The growth and decay of diffraction peaks with temperature signify changes in the phase of the material. Transformation temperatures obtained

Table 1 Transformation temperatures measured with in situ temperature dependent optical microscopy

Temp. (°C)	Time (min)	A_s (°C)	A_f (°C)	M_s (°C)	M_f (°C)
460	5	37.8	39.6	37.2	33.2
460	30	42.2	46.8	42.4	34.5
460	60	42.1	46.6	42.6	35.1
560	5	42.5	44.7	41.2	33.3
560	30	37.9	42.2	36.9	32.9
560	60	26.4	31	25.9	20.8
660	5	27.4	32	26.4	19.2

using this method are shown in Table 2. As observed in the optical transformation temperature measurements, some samples were not transformed even when cooled to 5°C, and thus transformation temperatures were not obtained for these samples. Since the X-rays are known to penetrate the entire thickness of the film, it can be concluded that no transformation is occurring for these

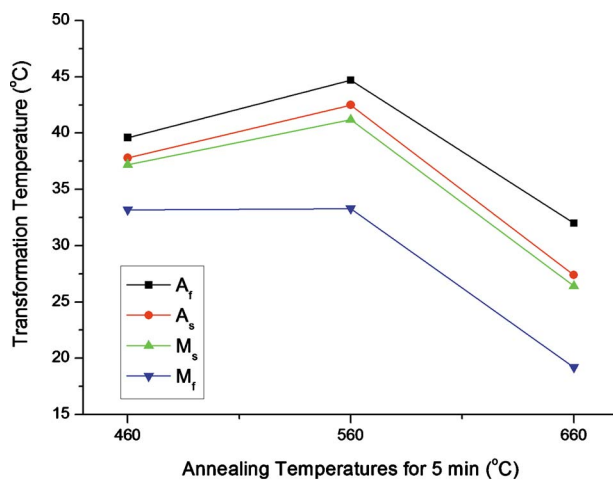


Fig. 5 Transformation temperatures versus annealing temperature for films annealed for 5 min. Measured through in situ temperature dependent optical microscopy. Transformation temperatures could not be measured for samples annealed at 760°C.

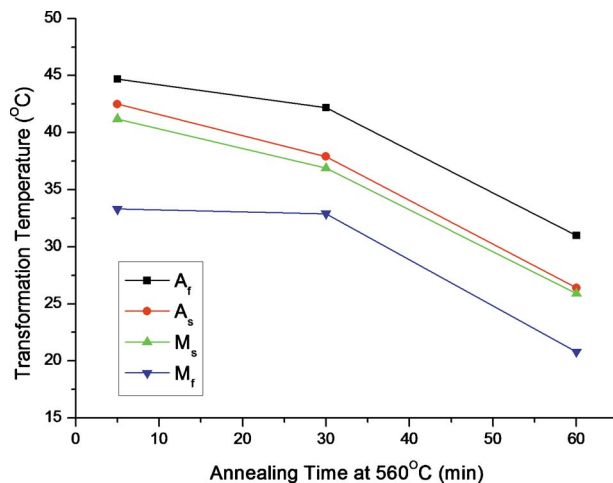


Fig. 6 Transformation temperatures versus annealing time for films annealed at 560°C. Measured through in situ temperature dependent optical microscopy. Transformation temperatures could not be measured for samples annealed at 760°C.

films. XRD spectra taken at room temperature for samples annealed for 5 min are shown in Fig. 7. Although no transformation was observed during cooling to 5°C, the existence of austenitic diffraction peaks rather than other non-shape memory phases in the high-temperature annealed samples suggests that increased driving force through further cooling could trigger the transformation to martensite. The growth of the austenitic peaks with increasing annealing temperature also signifies a decrease in transformation temperature with annealing temperature. Spectra for samples annealed at 560°C show a similar trend with time, as shown in Fig. 8. Similar to the temperatures measured through optical microscopy, the XRD transformation temperature measurements show a decreasing trend with both time and temperature, which is attributed to the change in matrix composition with precipitate growth.

4.4 Transformation Temperature—Surface and Volume.

While the two methods described above are measuring the same phenomenon, there are differences between the two measurements, most notably that the optical method only captures transformations occurring at the surface of the film, whereas the XRD method captures the transformation occurring throughout the thickness of the film. X-rays are known to be penetrating the entire thickness of the films since a diffraction peak from the silicon substrate is observed for large-range scans. Figures 9 and 10 show transformation temperatures for films annealed at 560°C and films annealed for 5 min, respectively, measured using both the XRD and optical methods. Comparing the transformation temperatures, it is clear that both are showing the same trend of decreasing transformation temperature with annealing temperature and time. Transformation temperatures measured using the optical method, however, are generally lower than those measured using XRD.

It has been shown by Wu et al. [19] that a residual stress gradient is formed through the thickness of annealed NiTi thin films with a larger residual stress existing at the film-substrate interface. As discussed previously, stresses in shape memory alloys can cause the transformation temperatures to change. Thus, due to the stress gradient in the film, the transformation temperatures are expected to vary in the thickness direction. Since increases in stress cause increases in transformation temperatures, parts of the film closer to the film-substrate interface would exhibit higher transformation temperatures than the film surface. Indeed, it is observed that, on average, the transformation temperatures of the volume of the film (XRD) are a few degrees higher than those measured using optical methods.

4.5 Mechanical Response.

As described previously, the transformation temperatures of SMAs have a significant effect on their response to loading. Depending on the initial structure of the film, the deformation induced by the indenter can be accommodated by different mechanisms. Films that are martensite at room temperature accommodate the indentation through elastic deformation of the martensite, detwinning, and plastic deformation of the martensite. The residual imprint left in the sample after the tip

Table 2 Transformation temperatures for annealed samples measured through in situ temperature dependent X-ray diffraction

Temp. (°C)	Time (min)	A_s (°C)	A_f (°C)	M_s (°C)	M_f (°C)
460	5	43.0	45.8	39.0	33.2
460	30	41.9	45.8	37.9	32.7
460	60	44.2	47.2	39.0	34.4
560	5	45.6	49.8	40.0	34.3
560	30	39.2	43.8	36.8	33.5
560	60	31.2	37.5	29.6	25.5
660	5	32.4	36.6	29.1	24.4

is retracted is the deformation accommodated by detwinning and plasticity. Films that are austenitic at room temperature accommodate the deformation initially by elastic deformation of the austenite, the stress-induced phase transformation to martensite, followed by elastic and plastic deformation of the martensite. Plastic deformation of the austenite can also be induced depending on the

level of stress required to cause the austenite to martensite phase transformation. For these films, the residual imprint is the deformation accommodated by the plasticity of the austenite or martensite and any residual stress-induced martensite left after

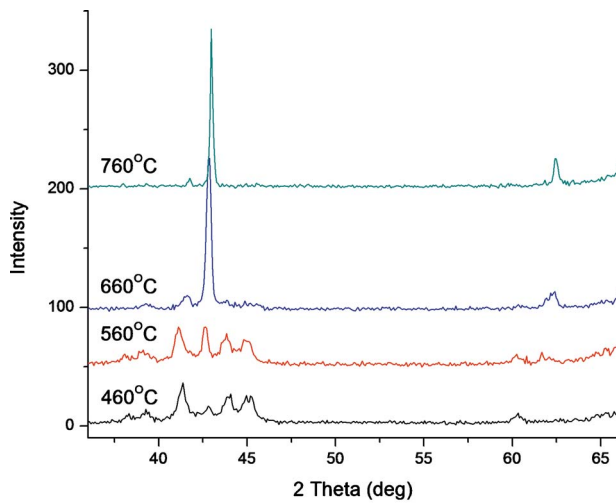


Fig. 7 XRD spectra for films annealed for 5 min at various temperatures. Note growth of austenitic peaks (42.8° and 61.8°) and decay of martensitic peaks with increasing annealing temperature. Spectra shifted for clarity.

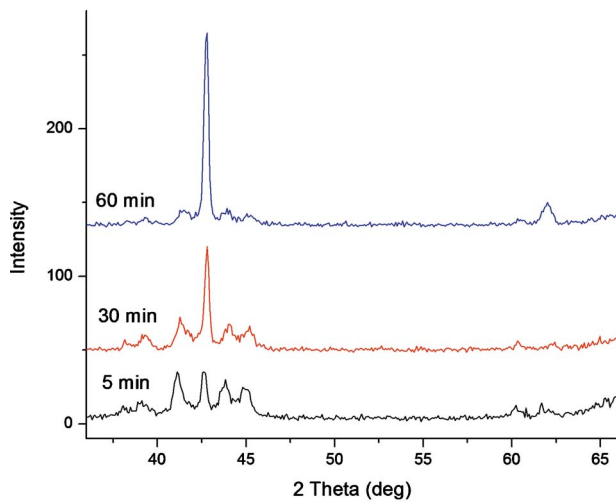


Fig. 8 XRD spectra for films annealed at 560°C for various times. Note growth of austenitic peaks (42.8 deg and 61.8 deg) and decay of martensitic peaks with increasing annealing time. Spectra shifted for clarity.

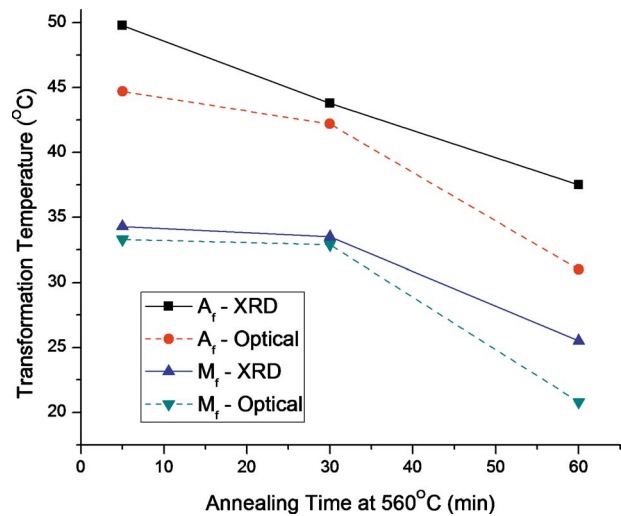


Fig. 9 Transformation temperatures of samples annealed at 560°C as a function of time. Comparison between XRD and optical methods. Austenitic start (A_s) and martensitic start (M_s) omitted for clarity.

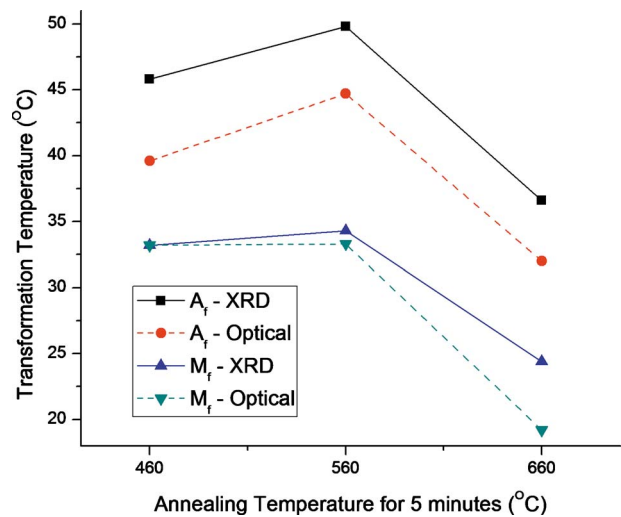


Fig. 10 Transformation temperatures of samples annealed for 5 min as a function of annealing temperature. Comparison between XRD and optical methods. Austenitic start (A_s) and martensitic start (M_s) omitted for clarity. Transformation temperatures could not be measured for samples annealed at 760°C.

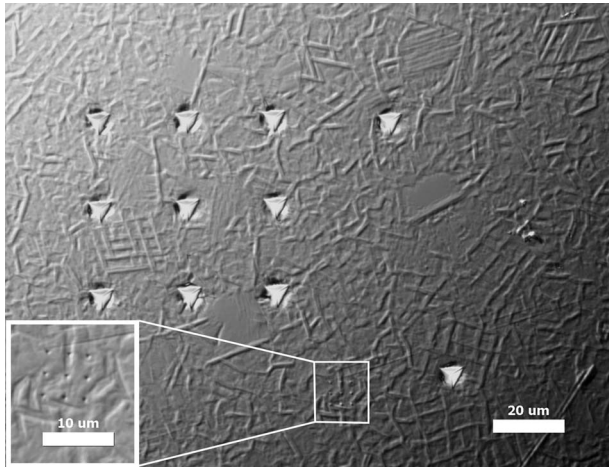


Fig. 11 Optical micrograph of residual impressions from 1 μm and 100 nm (inset) deep indentations on annealed NiTi film before heating. Film annealed at 460 $^{\circ}\text{C}$ for 5 min.

unloading.

Figure 11 is an optical micrograph of indentations made in a martensitic film, which was annealed at 460 $^{\circ}\text{C}$ for 5 min. The larger 3 \times 3 array is a set of 1 μm deep CSM indentations, while the smaller array (inset) consists of nine 100 nm deep basic indents. Surface relief typical of martensite is also visible over the entire film surface.

Figure 12 shows representative load-displacement curves for 100 nm basic indentations into martensitic and austenitic films. Arrays of both 100 nm basic and 1 μm CSM indentation tests were performed on all samples. The resulting indentation modulus and hardness of the films as a function of annealing temperature are shown in Fig. 13. An increase in both indentation modulus and hardness with annealing temperature is observed for all annealing times and is attributed to the decrease in transformation temperatures with annealing time. As the forward transformation temperatures drop below room temperature, the room temperature phase changes from martensite to austenite. The presence of austenite, a stiffer and harder phase, results in the observed changes.

Aside from the modulus and hardness of the films, a number of additional parameters of interest can be calculated directly from the load-displacement curves. The displacement at zero load on

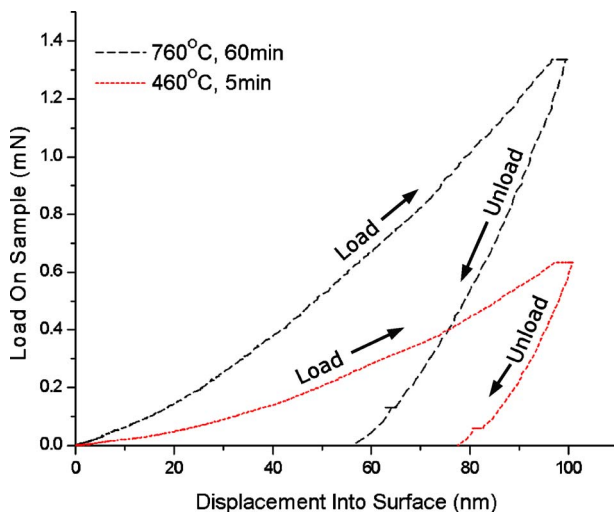


Fig. 12 Representative load-displacement curves for 100 nm indentation in annealed films. Note smaller residual indentation depth of austenitic film due to superelasticity.

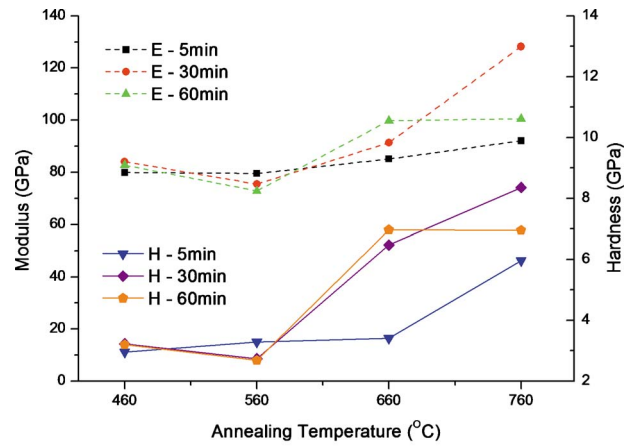


Fig. 13 Modulus and hardness of films annealed at various temperatures and times

the unloading curve gives a measure of the indentation depth remaining in the surface after removal of the indenter tip. The greater depth recovery upon unloading for the high-temperature annealed sample is attributed to the superelastic response expected from austenitic material and suggests that while not observed under cooling, the martensitic transformation does occur in this material. The reverse transformation from martensite to austenite, which occurs in the course of unloading for austenitic films, allows the films to recover a greater amount of the induced deformation prior to heating.

Additionally, the area within the load-unload curves represents the energy dissipated during the indentation. This value can be used to determine the dissipated energy ratio, which is defined as the dissipated energy divided by the total energy input, the total area under the loading curve. For a martensitic film, energy dissipation is caused by plastic deformation as well as detwinning. For an austenitic film, energy dissipation is caused solely by plastic deformation since any deformation accommodated by phase transformation is recoverable upon unloading.

The dissipated energy ratio for films annealed at various temperatures is shown in Fig. 14. The films annealed at lower temperatures, 460 $^{\circ}\text{C}$ and 560 $^{\circ}\text{C}$, show a large dissipated energy ratio of about 0.75. As the annealing temperature is increased, the dissipated energy ratio drops to near 0.6. This drop is considered to be due to the change in transformation temperatures of the films.

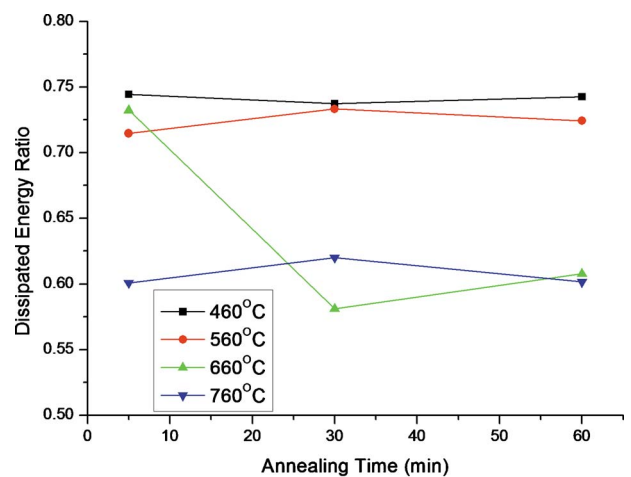


Fig. 14 Dissipated energy ratio versus annealing time at various temperatures. Note reduced dissipation for higher temperature heat treatments due to austenitic structure.

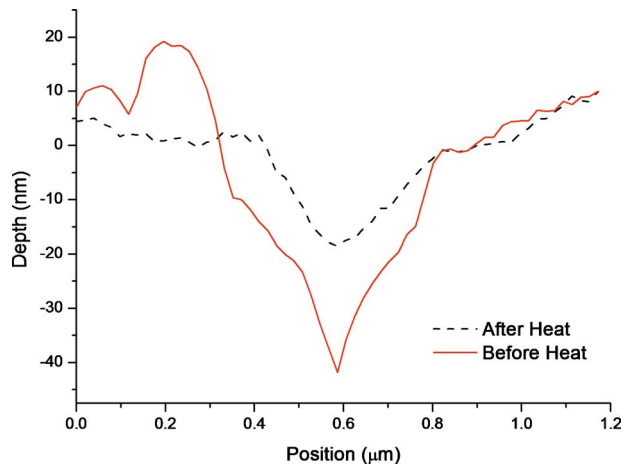


Fig. 15 Cross section of typical AFM scan of indentations in martensitic films before and after heating showing depth recovery. Film annealed at 460 °C for 5 min.

Since more energy is recovered in austenitic films due to the superelastic effect, they are expected to dissipate less energy during indentation. However, not all of the samples annealed at 660 °C exhibit the low dissipated energy ratio. The sample annealed for 5 min shows a ratio indistinguishable from the films annealed at 460 and 560 °C. This is also the only film annealed above 560 °C that shows any martensite at room temperature. The dissipated energy ratio is observed to be strongly related to the room temperature phase of the material and nearly constant for each phase.

4.6 Recoverable Depth. In addition to the material and shape memory properties derived from the indentation load-displacement curves, further characterization of the films can be achieved through a coupled nanoindentation-AFM experiment to determine the recoverable depth. Cross-section AFM scans of an indentation in a martensitic film before and after heating are shown in Fig. 15 and show clear depth recovery.

Figure 16 shows the effect of annealing temperature on the depth recovery ratio of films annealed for 5 min. A clear downward trend in recovery ratio is seen with increasing annealing temperature. This trend is due to a combination of effects including the shift in transformation temperatures as well as the change in precipitate shape as described in previous sections. Annealing

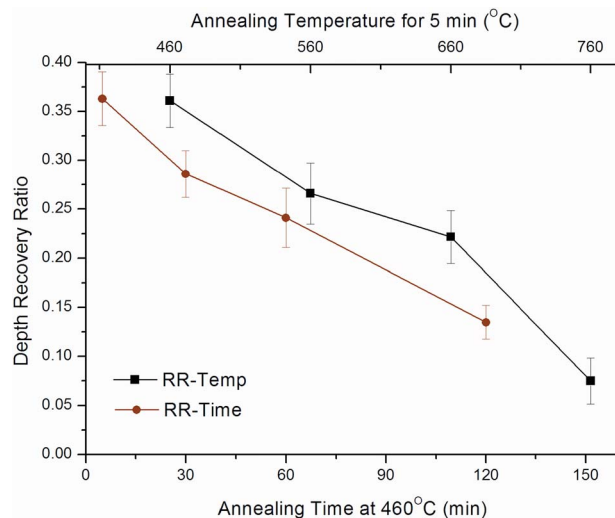


Fig. 16 Recovery ratio as a function of annealing temperature and time. Error bars denote standard error.

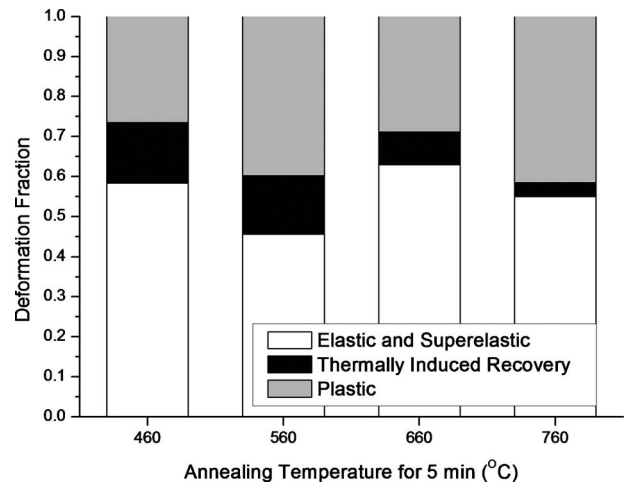


Fig. 17 Percentage of deformation accommodated by different mechanisms for films annealed for 5 min

at 460 °C produces a fully crystalline, fully martensitic film with GP zones rather than spherical precipitates. This combination produces the greatest level of depth recovery upon heating since the entire film is viable shape memory material and since GP zones have been shown to inhibit plastic deformation. Thus, the film is able to accommodate large transformation strains before reaching plasticity.

As discussed in previous sections, as the annealing temperature of the films is increased, a drop in transformation temperatures and a transition toward larger spherical precipitates occurs. A decrease in transformation temperatures can have the effect of increasing the critical stress for inducing martensite, as depicted in Fig. 1; however, for films that are martensitic at room temperature, this effect is very small. Instead, the reduced recovery experienced by the film annealed at 560 °C compared with the 460 °C case is attributed to the transition from GP zones to spherical precipitates, which have been shown to allow for greater plastic deformation. Considered in the context of Eq. (6), the decrease in recovery ratio at this temperature would be due to a decrease in Y_{pl} rather than an increase in Y_{mr} .

The presence of austenite in films annealed at higher temperatures, 660 °C and 760 °C, contributes to the further reduction in recovery ratio. The austenite in the films is not viable for the shape memory effect at room temperature and thus cannot contribute to the recovery of the indentation depth upon heating. In addition, the increase in the critical stress for phase transformation with decreasing transformation temperatures for the austenitic films could have the effect of increasing the amount of plasticity induced during indentation. Thus, the further decrease in depth recovery for the 660 °C and 760 °C cases is attributed primarily to the increase in Y_{mr} . The forward transformation temperatures of the 660 °C sample are close to room temperature, which suggests a low stress to induce the phase transformation. The 760 °C sample, however, did not transform even when cooled to 5 °C. This suggests a significantly higher critical stress for transformation, as expressed by Eq. (3). The dependence on Y_{pl} for lower temperature anneals and on Y_{mr} for higher temperature anneals agrees qualitatively with the observations by Murray [20] that the critical stress for slip in sputtered Ti-rich NiTi films is a decreasing function of heat treatment temperature up to 820 K and is nearly constant above that temperature.

The fractions of the induced deformation accommodated by the different mechanisms are shown in Fig. 17 as a function of temperature. As expected, among the martensitic films, the 560 °C samples show greater plastic deformation than the 460 °C samples, while among the austenitic films, the 760 °C samples

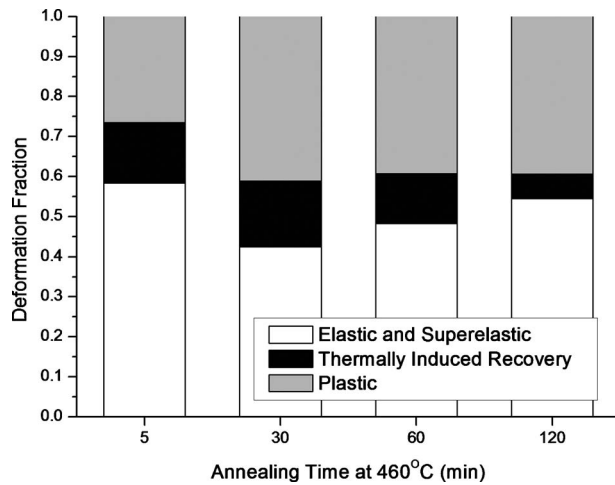


Fig. 18 Percentage of indentation deformation accommodated by different mechanisms as a function of annealing time at 460°C

show greater plastic deformation than the 660°C samples due to the increase in Y_{mr} . Overall, the thermally induced recovery decreases with annealing temperature due to the change in the room temperature phase from martensite to austenite. The elastic and superelastic deformation increases for the 660°C case due to the added deformation accommodated by superelasticity.

The effect of annealing time on the depth recovery ratio is also shown in Fig. 16 for films annealed at 460°C and shows a trend of decreasing depth recovery with increasing annealing time. In this case, however, all of the films are martensite at room temperature. Thus, the stress required for phase transformation and the percentage of viable shape memory material in the films are not expected to differ significantly between samples. Rather, the decrease in recovery ratio with annealing time is expected due to the effects of the precipitates within the grains. The strengthening effect of the GP zones created at lower annealing temperatures increases the critical stress for slip, which results in a larger depth recovery. As the films transition toward spherical precipitates, this strengthening effect lessens, decreasing Y_{pl} and reducing the depth recovery.

The fractions of the induced deformation accommodated by the different mechanisms for the samples annealed at 460°C are shown in Fig. 18. The low level of plastic deformation is clearly seen for the film annealed for 5 min due to expected strengthening by the GP zones. The level of plastic deformation is nearly constant for annealing times beyond 5 min; however, the level of thermally induced recovery begins to decrease. This decrease in thermally induced recovery could be attributed to increased Y_{mr} due to the limited growth of martensitic variants in films with spherical precipitates.

Similar trends were observed for films annealed at 660°C and 760°C as a function of time and for films annealed for 30 min and 60 min as a function of temperature (not shown). With overall decreases in the transformation temperatures with increasing annealing time and temperature, the stress required to induce the transformation keeps increasing. This results in, first, a transition between shape memory and superelastic responses and, second, increases in the level of plasticity experienced by the films and decreases in the depth recovery ratio.

5 Conclusion

The effects of heat treatment temperature and time on the resulting mechanical and shape memory properties of Ti-rich, amorphous NiTi films have been examined. The heat treatments resulted in both martensitic and austenitic films for different

annealing parameters, which demonstrates a significant shift in the transformation temperatures of the material. Transformation temperatures have been shown to decrease as a function of heat treatment time and temperature, which is attributed to the development of GP zones and spherical precipitates within the NiTi grains and the corresponding decrease in the Ti content of the matrix. It has also been observed that matrix composition has a more significant effect than precipitate size and distribution for the shorter heat treatments performed in this study. The mechanical response of films under indentation revealed increases in the critical stress for slip for films containing GP zones as well as a step decrease in dissipated energy between martensitic and austenitic films. The results described above demonstrate that short term aging treatments are a viable mechanism to tailor the mechanical and shape memory response of amorphous Ti-rich NiTi films.

Acknowledgment

Financial support provided by Columbia University is appreciated. Assistance in thin film preparation by Dr. X. Huang and Professor A. G. Ramirez of Yale University is gratefully acknowledged.

References

- [1] Bellourad, Y., 2008, "Shape Memory Alloys for Microsystems: A Review From a Material Research Perspective," *Mater. Sci. Eng., A*, **481-482**, pp. 582-589.
- [2] Ishida, A., Takei, A., and Miyazaki, S., 1993, "Shape Memory Thin Film of Ti-Ni Formed by Sputtering," *Thin Solid Films*, **228**, pp. 210-214.
- [3] Lee, H., Ni, H., Wu, D. T., and Ramirez, A. G., 2005, "Grain Size Estimations From the Direct Measurement of Nucleation and Growth," *Appl. Phys. Lett.*, **87**, p. 124102.
- [4] Paula, A. S., Canejo, J. P. H. G., Martins, R. M. S., and Fernandes, B., 2004, "Effect of Thermal Cycling on the Transformation Temperature Ranges of a Ni-Ti Shape Memory Alloy," *Mater. Sci. Eng., A*, **378**, pp. 92-96.
- [5] Ishida, A., Sato, M., and Miyazaki, S., 1999, "Mechanical Properties of Ti-Ni Shape Memory Thin Films Formed by Sputtering," *Mater. Sci. Eng., A*, **273-275**, pp. 754-757.
- [6] Firstov, G. S., Vitchev, R. G., Kumar, H., Blanpain, B., and Van Humbeeck, J., 2002, "Surface Oxidation of NiTi Shape Memory Alloy," *Biomaterials*, **23**, pp. 4863-4871.
- [7] Gall, K., Dunn, M. L., Liu, Y., Sehitoglu, H., and Chumlyakov, Y. I., 2002, "Micro and Macro Deformation of Single Crystal NiTi," *J. Eng. Mater. Technol.*, **124**, pp. 238-245.
- [8] Tall, P. D., Ndiaye, S., Beye, A. C., Zong, Z., Soboyejo, W. O., Lee, H., Ramirez, A. G., and Rajan, K., 2007, "Nanoindentation of Ni-Ti Thin Films," *Mater. Manuf. Processes*, **22**, pp. 175-179.
- [9] Shaw, G. A., and Crone, W. C., 2004, "Direct Measurement of the Nanoscale Mechanical Properties of NiTi Shape Memory Alloy," *Materials Research Society Symposium Proceedings: Mechanical Properties of Nanostructured Materials and Noncomposites*, Boston, MA, Vol. 791, pp. 215-220.
- [10] Kajiwara, S., Kikuchi, T., Ogawa, K., Matsunaga, T., and Miyazaki, S., 1996, "Strengthening of Ti-Ni Shape-Memory Films by Coherent Subnanometric Plate Precipitates," *Philos. Mag. Lett.*, **74**, pp. 137-144.
- [11] Shimizu, K., and Tadaki, T., 1987, "Shape Memory Effect: Mechanism, *Shape Memory Alloys*, H. Funakubo, ed., Gordon and Breach Science, New York, pp. 1-60.
- [12] Hill, R., 1950, *The Mathematical Theory of Elasticity*, Oxford University Press, Oxford, pp. 97-101.
- [13] Johnson, K. L., 1985, *Contact Mechanics*, Cambridge University Press, Cambridge, UK, pp. 171-175.
- [14] Shaw, G. A., Stone, D. S., Johnson, A. D., Ellis, A. B., and Crone, W. C., 2003, "Shape Memory Effect in Nanoindentation of Nickel-Titanium Thin Films," *Appl. Phys. Lett.*, **83**(2), pp. 257-259.
- [15] Zhang, Z. X., Sato, M., and Ishida, A., 2002, "Influence of Guinier-Preston Zones on Deformation in Ti-Rich Ti-Ni Thin Films," *Philos. Mag. Lett.*, **82**(5), pp. 257-264.
- [16] Ishida, A., Sato, M., Kimura, T., and Sawaguchi, T., 2001, "Effects of Composition and Annealing on Shape Memory Behavior of Ti-Rich Ti-Ni Thin Films Formed by Sputtering," *Mater. Trans.*, **42**(6), pp. 1060-1067.
- [17] Eckelmeyer, K. H., 1976, "The Effect of Alloying on the Shape Memory Phenomenon in Nitinol," *Scr. Metall.*, **10**, pp. 667-672.
- [18] Ishida, A., Sato, M., Takei, A., and Miyazaki, S., 1995, "Effect of Heat Treatment on Shape Memory Behavior of Ti-Rich Ti-Ni Thin Films," *Mater. Trans., JIM*, **36**, pp. 1349-1355.
- [19] Wu, T., Jiang, B., Qi, X., Liu, Y., Xu, D., and Wang, L., 2002, "Residual Stress in TiNi Shape Memory Alloy Thin Films With (111) Single-Crystal Silicon Wafer," *Mater. Trans., JIM*, **43**, pp. 566-570.
- [20] Murray, J. L., 1991, "Ni-Ti (Nickel-Titanium)," *Phase Diagrams of Binary Nickel Alloys*, P. Nash, ed., ASM International, Materials Park, OH, pp. 342-355.